


Cite this: *RSC Adv.*, 2023, 13, 8873

Interface engineering of CeO₂ nanoparticle/Bi₂WO₆ nanosheet nanohybrids with oxygen vacancies for oxygen evolution reactions under alkaline conditions†

Dukhyun Nam,^a Geunhyeong Lee^a and Jooheon Kim^{abc}

Because of the interactive combination synergy effect, hetero interface engineering is used way for advancing electrocatalytic activity and durability. In this study, we demonstrate that a CeO₂/Bi₂WO₆ heterostructure is synthesized by a hydrothermal method. Electrochemical measurement results indicate that CeO₂/Bi₂WO₆ displays not only more OER catalytic active sites with an overpotential of 390 mV and a Tafel slope of 117 mV dec⁻¹ but also durability for 10 h (97.57%). Such outstanding characteristics are primarily attributed to (1) the considerable activities by CeO₂ nanoparticles uniformly distributed on Bi₂WO₆ nanosheets and (2) the plentiful Bi–O–Ce and W–O–Ce species playing the role of strong couples between CeO₂ nanoparticles and Bi₂WO₆ nanosheets and oxygen vacancy existence in CeO₂ nanoparticles, which can improve the electrochemical active surface area (ECSA) and activity, and enhance the conductivity for OERs. This CeO₂/Bi₂WO₆ consists of the heterojunction engineering that can open a modern method of thinking for high effective OER electrocatalysts.

Received 28th December 2022

Accepted 26th February 2023

DOI: 10.1039/d2ra08273j

rsc.li/rsc-advances

1. Introduction

The energy demands and increasing environmental problem lead to a lot of research efforts in studying exchangeable conversion system and energy storage.^{1–6} The oxygen evolution reaction (OER) is key to the progress of renewable energy devices such as water-splitting devices and metal–air batteries.^{7–17} At the anode, the even work of the OER depends on catalyst engineering owing to its essentially sluggish reaction kinetics and multielectron transfer paths.^{18–22} Generally, noble metal oxides such as IrO₂ and RuO₂ are well-known electrocatalysts for OERs.^{23–27} However, their high price, serious scarcity, and unsatisfied stability of electrocatalysts are greatly frustrating in that they are more widely applied to a variety of energy devices. Therefore, it is crucial to explore effective, low-cost, abundant, and robust OER catalysts on Earth.

One of the easiest members of the Aurivillius family, bismuth tungstate (Bi₂WO₆) has become an outstanding OER electrocatalyst because of its abundant, low cost, clean properties, and excellent chemical stability.^{28–31} In detail, two-

dimensional Bi₂WO₆ nanosheets have a distinctive layer form and large specific surface area. These are useful to charge transfer, electrolyte penetration as well as active site exposure, regarded as a favorable catalyst support.^{32,33} Nonetheless, by the self-aggregating motion, Bi₂WO₆ nanosheets are simply aggregated to limit and decrease the electrochemically active region, indicating that the catalytic activity of OER is low.³⁰ According to the surface structure, the adsorption actions of reaction region and charge distribution are crucial to the electrochemical catalytic action.³⁴ Therefore, the interface engineering of heterostructures has been regarded as an effective strategy for optimizing the catalyst activities.^{35–40} The close connections between different active species in engineering interfaces optimize the powerful synergistic effect, rapid charge transfer rate and activation energy, and adsorption for intermediates, overcoming the shortcomings of single ingredient materials,^{36–38} whereas the heterointerfaces usually involve structural modification such as edges and dislocations as well as atomic defects including cation and anion vacancies, forming more active sites on the surface of the catalyst.⁴¹ To accomplish this aim, it is essential to choose appropriate introduced species that form the optimal electrocatalysts. Due to its chemical properties and unique electronic structure, CeO₂ has been extensively studied as an effective supporter of the OER. The abundant oxygen vacancies of CeO₂ and flexible conversion between Ce³⁺ and Ce⁴⁺ can enable several moving oxygen atoms to access active sites as an oxygen buffer for the effective absorption of oxygen species.^{42–47} Thus, we think that the hybridization of Bi₂WO₆

^aSchool of Chemical Engineering & Materials Science, Chung-Ang University, 84 Heukseok-ro, Dongjak-gu, Seoul, Korea. E-mail: jooheonkim@cau.ac.kr

^bDepartment of Advanced Materials Engineering, Chung-Ang University, Anseong-si, Gyeonggi-do 17546, Republic of Korea

^cDepartment of Intelligent Energy and Industry, Graduate School, Chung-Ang University, Seoul 06974, Republic of Korea

† Electronic supplementary information (ESI) available. See DOI: <https://doi.org/10.1039/d2ra08273j>


and CeO_2 has to be a reasonable tactic to enhance the OER activity by the interface engineering.

In this work, we manufacture a modern sort of $\text{CeO}_2/\text{Bi}_2\text{WO}_6$ heterostructure consisting of CeO_2 nanoparticles on Bi_2WO_6 nanosheets by a hydrothermal method for OER electrocatalysts in alkaline media. The excellent electrocatalytic active site and durability come from the distinct heterostructure and combined interface synergistic effect with equally distributed CeO_2 nanoparticles fixing Bi_2WO_6 nanosheets, which disclose more activity, have charge transfer rates, and show steady heterostructures. At the heterostructure, this approach *via* bonding the shape plan and electronic transformation fulfills advancement of catalysts, which supply direction for using activity encouraging and high effectiveness and stability OER electrocatalysts.

2. Experiment method

2.1. Synthesis of Bi_2WO_6 nanosheets

First, 0.05 g hexadecyltrimethylammonium bromide (CTAB) (0.1 mmol) was dispersed in 80 ml deionized water under stirring for 10 minutes. Then, 0.917 g $\text{Bi}(\text{NO}_3)_3 \cdot 5\text{H}_2\text{O}$ was added to the obtained solution for 30 minutes. Finally, 0.33 g $\text{Na}_2\text{WO}_4 \cdot 2\text{H}_2\text{O}$ was added to the solution and stirred for 30 minutes. Afterward, the as-obtained solution was transferred to a 100 ml Teflon-lined hydrothermal autoclave, which was then maintained at 120 °C for 24 hours. Finally, the precursor was washed several times with deionized water and dried at 50 °C overnight.

2.2. Synthesis of $\text{CeO}_2/\text{Bi}_2\text{WO}_6$ nanohybrids

First, 1 mmol $\text{Ce}(\text{NH}_4)_2(\text{NO}_3)_6$ (0.5482 g) was added into 50 ml deionized water under a stirring process for 30 minutes. Then, 0.5 mmol Bi_2WO_6 (0.3488 g) was added to this solution and ultrasonicated until complete dissolution. After sonication, 10 ml of NaBH_4 solution (0.05 M) was added to the solution. The product was washed several times with ethanol and deionized water and dried at 50 °C overnight. After drying overnight, the as-prepared sample was calcined at 420 °C for 2 hours.

2.3. Synthesis of CeO_2 nanoparticles

The synthesis of CeO_2 is similar to that of the $\text{CeO}_2/\text{Bi}_2\text{WO}_6$ nanohybrid except for the additional treatment. To be more specific, although other experimental methods remain the same, only the second process of the $\text{CeO}_2/\text{Bi}_2\text{WO}_6$ nanohybrid synthesis method was excluded.

3. Results and discussion

Fig. 1 describes the process of formation of $\text{CeO}_2/\text{Bi}_2\text{WO}_6$ nanohybrids *via* a hydrothermal reaction. The first process began with use of hydrothermal synthesis of Bi_2WO_6 nanosheets. The Br-ion CTAB bound on the Bi_2WO_6 surface can adsorb positively charged Ce^{4+} ions.^{31,48} Next, Ce^{4+} ions were easily reduced to CeO_2 nanoparticles by forming nanohybrids of $\text{CeO}_2/\text{Bi}_2\text{WO}_6$ using NaBH_4 as a reducing agent accumulated on the Bi_2WO_6 nanosheet.³¹ During the experiment, Bi-ions and W-

ions could be reduced by NaBH_4 that obtains the advantages of Bi–O–Ce, W–O–Ce bond formation by substituting Br[−] to Ce–O[−]. The $\text{CeO}_2/\text{Bi}_2\text{WO}_6$ nanohybrid was annealed at 420 °C in air, and thus, stable fixed CeO_2 nanoparticles were bonded to the Bi_2WO_6 surface. The NaBH_4 reduction was selected because it is easy to perform and inexpensive for the manufacture of vacancies. In addition, it generates many defects for exposing more reactive sites and increases the conductivity.⁴⁹

3.1. Morphology and structure of $\text{CeO}_2/\text{Bi}_2\text{WO}_6$

The morphology and microstructure of the prepared samples were analyzed by FE-SEM, as shown in Fig. S1, S2† and 2. As shown in Fig. S1a and b (ESI†), the microstructure of the CeO_2 sample was characterized by nanoparticles. The morphology of Bi_2WO_6 showed nanosheet features, as shown in Fig. S2a and b (ESI†). After addition of NaBH_4 and $\text{Ce}(\text{NH}_4)_2(\text{NO}_3)_6$ and calcination at 420 °C for 2 hours, $\text{CeO}_2/\text{Bi}_2\text{WO}_6$ could not change the structure of Bi_2WO_6 nanosheets (Fig. 2), which implies that the microstructure of Bi_2WO_6 could be maintained by the addition of NaBH_4 and $\text{Ce}(\text{NH}_4)_2(\text{NO}_3)_6$ and calcination could keep the microstructure of Bi_2WO_6 . In addition, the surface nanoparticles cannot be found on the $\text{CeO}_2/\text{Bi}_2\text{WO}_6$ nanohybrid due to the low loading and uniform growth on the Bi_2WO_6 nanosheet of CeO_2 nanoparticles.^{28,29} Meanwhile, the irregular nanoparticles on the surface could be distinguished from the surface of the Bi_2WO_6 nanosheets. This suggests that the CeO_2 nanoparticles were successfully fixed and uniformly grown on the Bi_2WO_6 nanosheets. The distinctive heterostructure provided strong electron interaction and interfacial synergy between Bi_2WO_6 nanosheets and CeO_2 nanoparticles, which is important for adjusting the electronic structure and exposing several active sites to increase the electrocatalytic activity and durability of electrocatalysts.^{50,51}

To further examine the structure of CeO_2 nanoparticles on the surface of Bi_2WO_6 nanosheets, the crystal structure of CeO_2 , Bi_2WO_6 , and $\text{CeO}_2/\text{Bi}_2\text{WO}_6$ was investigated by FE-TEM analysis, as shown in Fig. S3, S4† and 3. As illustrated in Fig. S3a and b,† the FE-TEM images displayed CeO_2 with nanoparticle structure, implying that the CeO_2 nanoparticles were synthesized. The HRTEM image of CeO_2 indicated that the *d*-spacing of the lattice fringes is 0.271 and 0.312 nm, corresponding to the (200) and (111) planes, respectively, as shown in Fig. S3c†.⁵² Meanwhile, the FE-TEM images represented Bi_2WO_6 with a sheet-like form, and the nanosheets can be seen in Fig. S4a and b,† showing that Bi_2WO_6 nanosheets were synthesized. As shown in Fig. S4c,† the HRTEM image shows that the *d*-space of lattice fringes is 0.272 nm, corresponding to the (020) plane of

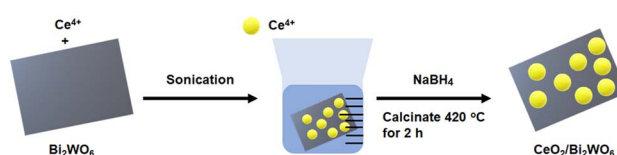


Fig. 1 Schematic illustration of synthesis process of $\text{CeO}_2/\text{Bi}_2\text{WO}_6$ nanohybrids.



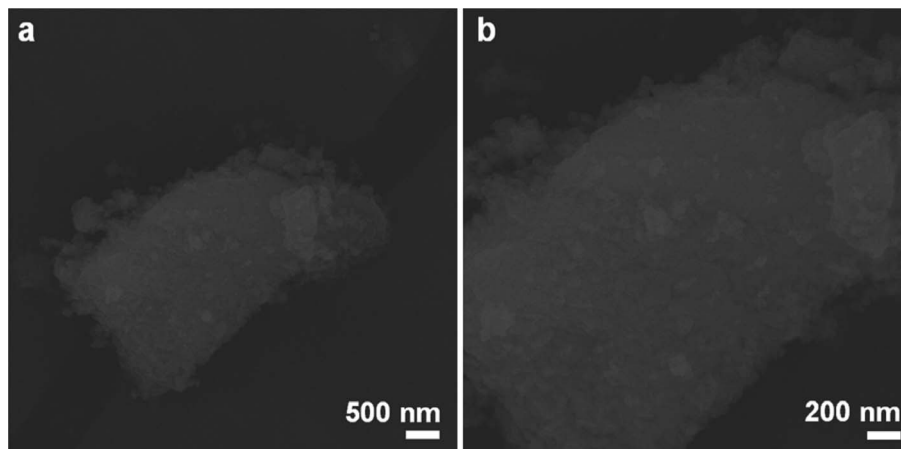


Fig. 2 FE-SEM images at (a) low magnification and (b) high magnification of $\text{CeO}_2/\text{Bi}_2\text{WO}_6$ nanohybrids.

Bi_2WO_6 .⁵³ The FE-TEM images of $\text{CeO}_2/\text{Bi}_2\text{WO}_6$ nanohybrids are displayed in Fig. 3a and b. The $\text{CeO}_2/\text{Bi}_2\text{WO}_6$ sample was large and had nanosheet properties, and irregular CeO_2 nanoparticles were dispersed on the Bi_2WO_6 nanosheets. In addition, it could be found that some nanoparticles were spread out on the Bi_2WO_6 nanosheets, confirming that the CeO_2 nanoparticles were grown on the Bi_2WO_6 nanosheets, which is consistent with the FE-SEM results.⁵⁴ Fig. 3c shows the HRTEM image of the $\text{CeO}_2/\text{Bi}_2\text{WO}_6$ nanohybrid catalyst, and the lattice edges of CeO_2 nanoparticles and Bi_2WO_6 nanosheets might be surely differentiated, and the lattice edges of 0.271 nm, 0.312 nm, and 0.272 nm corresponded to the (200) and (101) planes of CeO_2 and the (020) plane of Bi_2WO_6 , respectively. Finally, to investigate the elemental composition of $\text{CeO}_2/\text{Bi}_2\text{WO}_6$ nanohybrids catalyst, the energy dispersive X-ray

spectrometry (EDS) was perfected in Fig. 3e. The four elements of Ce, Bi, W, and O were uniformly distributed over the whole $\text{CeO}_2/\text{Bi}_2\text{WO}_6$ nanohybrid catalyst, which suggested that the CeO_2 nanoparticles combined with the surface of Bi_2WO_6 nanosheets, confirming that the CeO_2 nanoparticle/ Bi_2WO_6 nanosheet heterostructure was successfully synthesized.

To confirm the crystal structure and phase composition of $\text{CeO}_2/\text{Bi}_2\text{WO}_6$, CeO_2 , and Bi_2WO_6 catalysts, we conducted X-ray diffraction (XRD), as shown in Fig. 4a. The peaks at 28.7° , 33.3° , 47.6° , 56.5° , 59.3° , and 69.5° corresponded to the (111), (200), (220), (311), (222), and (400) planes of CeO_2 , respectively. These results were consistent with the CeO_2 crystal structure (JCPDS No. 81-0792).⁵⁵ Similarly, the diffraction peaks of $\text{CeO}_2/\text{Bi}_2\text{WO}_6$ and Bi_2WO_6 matched JCPDS No. 73-2020 of Bi_2WO_6 .⁵⁶ In addition, no diffraction peaks were studied from other materials.

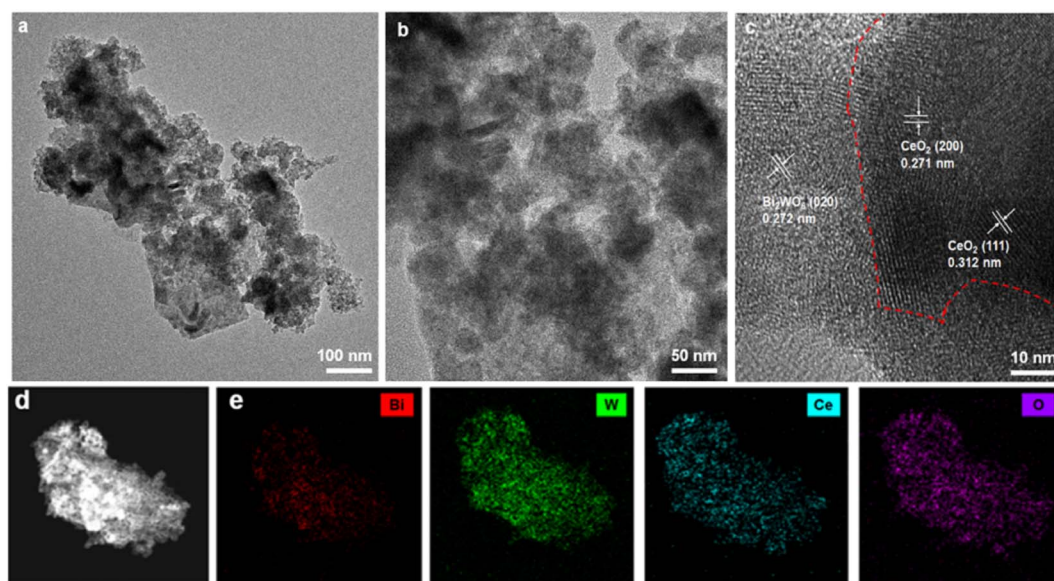


Fig. 3 FE-TEM images at (a) low magnification and (b) high magnification of $\text{CeO}_2/\text{Bi}_2\text{WO}_6$ nanohybrids. (c) HRTEM image of $\text{CeO}_2/\text{Bi}_2\text{WO}_6$ nanohybrids. (d) Dark-field FE-TEM image of $\text{CeO}_2/\text{Bi}_2\text{WO}_6$ nanohybrids. (e) EDS mapping images for Bi, W, Ce, and O elements distributed at $\text{CeO}_2/\text{Bi}_2\text{WO}_6$ nanohybrids.

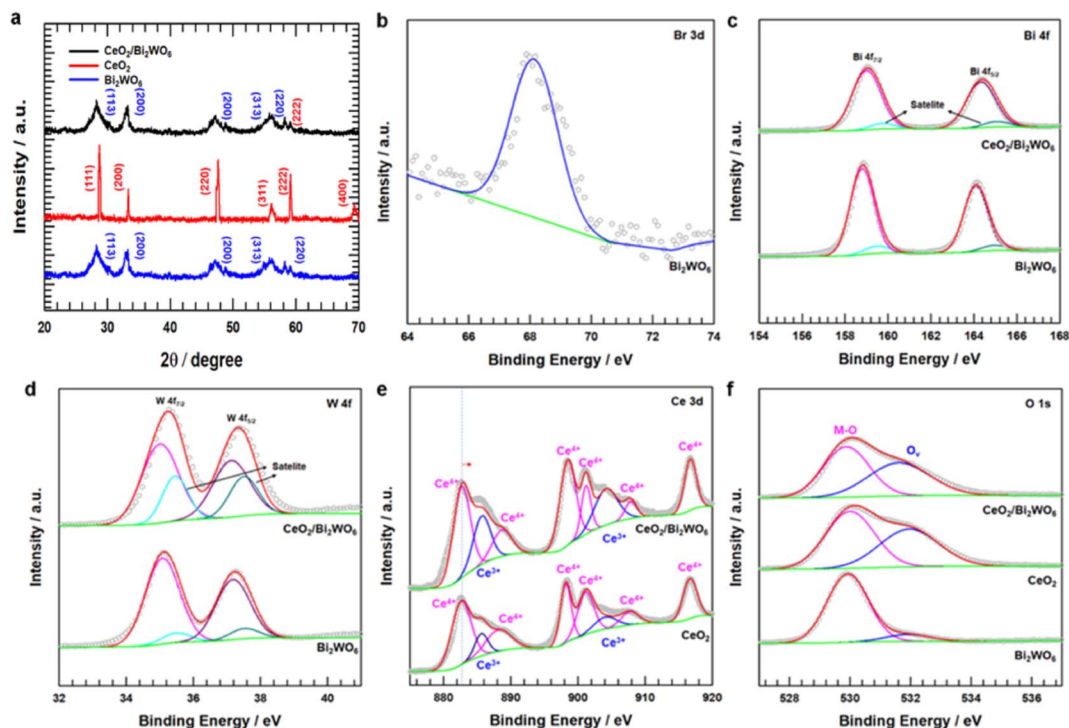


Fig. 4 (a) XRD pattern of $\text{CeO}_2/\text{Bi}_2\text{WO}_6$ and $\text{CeO}_2/\text{Bi}_2\text{WO}_6$. (b) XPS Br 3d deconvolution spectrum of Bi_2WO_6 . (c) XPS Bi 4f deconvolution spectrum of Bi_2WO_6 and $\text{CeO}_2/\text{Bi}_2\text{WO}_6$. (d) XPS W 4f deconvolution spectrum of Bi_2WO_6 and $\text{CeO}_2/\text{Bi}_2\text{WO}_6$. (e) XPS Ce 3d deconvolution spectrum of CeO_2 and $\text{CeO}_2/\text{Bi}_2\text{WO}_6$. (f) XPS O 1s deconvolution spectrum of CeO_2 , Bi_2WO_6 and $\text{CeO}_2/\text{Bi}_2\text{WO}_6$.

This might be the surface of the Bi_2WO_6 nanosheets of the CeO_2 nanoparticles due to low loading and even growth.^{29–31}

To identify the chemical valence states and surface elemental contents, the X-ray photoelectron (XPS) spectra recorded for CeO_2 , Bi_2WO_6 , and $\text{CeO}_2/\text{Bi}_2\text{WO}_6$ are shown in Fig. S5† and 4b–f. As shown in Fig. S5†, the XPS survey spectrum indicated the existence of Ce, Bi, W, and O elements, in accordance with the above-mentioned XRD result (Fig. 4a). Fig. 4b–f displays the high-resolution spectra of Br 3d, Bi 4f, W 4f, Ce 3d and O 1s, respectively. In the case of pure Bi_2WO_6 , the binding energies of the Br 3d peak were determined to be 68.6 eV, as shown in Fig. 4b, confirming that the Br ions of CTAB were bound to the surface Bi and W atoms of Bi_2WO_6 .⁵³ As shown in

Fig. 4c, Bi_2WO_6 and $\text{CeO}_2/\text{Bi}_2\text{WO}_6$ could be divided into two Bi 4f peaks. The properties of Bi 4f_{5/2} and Bi 4f_{7/2} were two peaks at 164.3 and 159.2 eV that matched Bi³⁺ ions of Bi_2WO_6 .⁵⁷ The shoulder peaks Bi 4f_{5/2} and Bi 4f_{7/2}, corresponding to 165.6 and 160.6 eV, appeared at a higher binding energy. The peaks of Bi, represented at a higher energy, meant that the Bi atoms had higher electrical positivity in binding with the surface Br atoms.^{53,57} Similarly, for the high-resolution XPS W 4f spectrum (Fig. 4d), 4f_{7/2} and 4f_{5/2} electron orbits of W⁶⁺ corresponded to two feature peaks at 35.2 eV and 37.3 eV, respectively. In addition, the orbits of W 4f_{7/2} and W 4f_{5/2} belonged to the satellite peaks at 35.6 eV and 37.6 eV, respectively. Compared to Bi_2WO_6 , the binding energy of $\text{CeO}_2/\text{Bi}_2\text{WO}_6$ was moved slightly to the

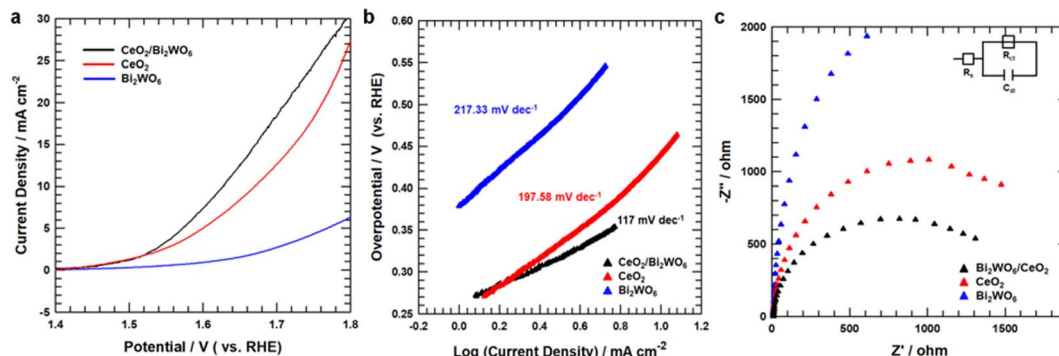


Fig. 5 (a) OER LSV curves for CeO_2 , Bi_2WO_6 , and $\text{CeO}_2/\text{Bi}_2\text{WO}_6$ in a N_2 -saturated 1.0 M KOH electrolyte. (b) Tafel plots for CeO_2 , Bi_2WO_6 , and $\text{CeO}_2/\text{Bi}_2\text{WO}_6$. (c) Nyquist plots for CeO_2 , Bi_2WO_6 , and $\text{CeO}_2/\text{Bi}_2\text{WO}_6$ recorded at 1.65 V.



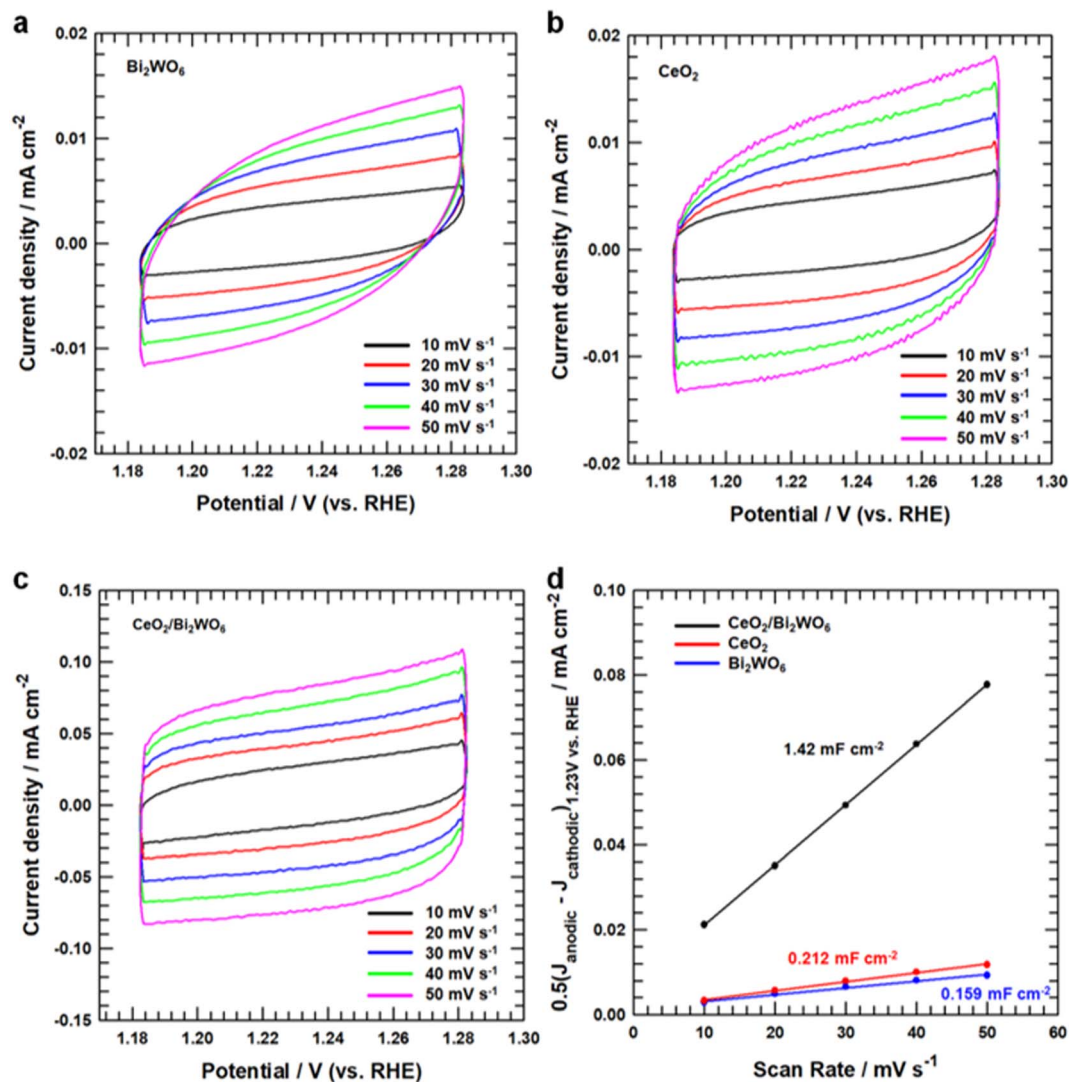


Fig. 6 CV curves (a) CeO_2 , (b) Bi_2WO_6 , and (c) $\text{CeO}_2/\text{Bi}_2\text{WO}_6$ in a non-faradaic current region (1.18–1.28 V vs. RHE) at different scan rates of 10, 20, 30, 40, and 50 mV s^{-1} . (d) Linear fitting of the capacitive currents versus CV scan rates of CeO_2 , Bi_2WO_6 , and $\text{CeO}_2/\text{Bi}_2\text{WO}_6$.

negative parts, confirming that the electropositive W appearing on the Bi_2WO_6 nanosheets was increasingly higher.^{28,53} The high-resolution XPS Ce 3d spectrum for $\text{CeO}_2/\text{Bi}_2\text{WO}_6$ was composed with the peaks compared to CeO_2 (Fig. 4e). The Ce 3d spectrum of $\text{CeO}_2/\text{Bi}_2\text{WO}_6$ and CeO_2 samples could be separated into eight peaks, two peaks were assigned to Ce^{3+} at 885.7 and 904.2 eV, and six peaks were assigned to Ce^{4+} at 882.7, 888.7, 898.5, 901.2, 907.9, and 916.7 eV for $\text{CeO}_2/\text{Bi}_2\text{WO}_6$.⁵⁸ According to the Ce 3d spectrum analysis, Ce^{3+} and Ce^{4+} were present in CeO_2 and $\text{CeO}_2/\text{Bi}_2\text{WO}_6$. For the Ce 3d spectrum, it might be observed that CeO_2 and $\text{CeO}_2/\text{Bi}_2\text{WO}_6$ were plentiful in Ce^{3+} species, which showed the formation of oxygen vacancies in these two samples.⁵⁸ Besides, the binding energy of the Ce 3d spectrum in $\text{CeO}_2/\text{Bi}_2\text{WO}_6$ had a clear positive change compared to CeO_2 . The suitable electron structure of $\text{CeO}_2/\text{Bi}_2\text{WO}_6$ could help to enhance the catalyst's OER performance by inducing charge redistribution at the interface.^{59,60} Fig. 4f shows the two peaks for the O 1s spectrum. The O 1s peak at

530.2 eV was attributed to the oxygen atom bonded to the metal, and the center position at 532.1 eV was ascribed to the oxygen atom in the surrounding area of oxygen vacancies.⁶¹ However, according to the feature peak, the peak area at 532.1 eV varied greatly, which displayed that the $\text{CeO}_2/\text{Bi}_2\text{WO}_6$ nanohybrids had much more oxygen vacancies. Interestingly, as shown in Table S1,† the $\text{CeO}_2/\text{Bi}_2\text{WO}_6$ nanohybrids (46.8%) is higher than that of CeO_2 nanoparticles (44.6%) and Bi_2WO_6 nanosheets (9.7%). These results indicated that the $\text{CeO}_2/\text{Bi}_2\text{WO}_6$ nanohybrids had enough oxygen vacancies. As a result, the CeO_2 nanoparticles abundant in evenly grown oxygen vacancies on Bi_2WO_6 nanosheets were successfully synthesized.

3.2. Oxygen electrochemical performance of electrocatalysts

To study the OER catalytic active sites of all samples, we studied the electrochemical characteristics of $\text{CeO}_2/\text{Bi}_2\text{WO}_6$, CeO_2 , and Bi_2WO_6 for OERs in alkaline solutions (pH = 14) using a rotating disk electrode (RDE) (see Detail Methods in the ESI†).

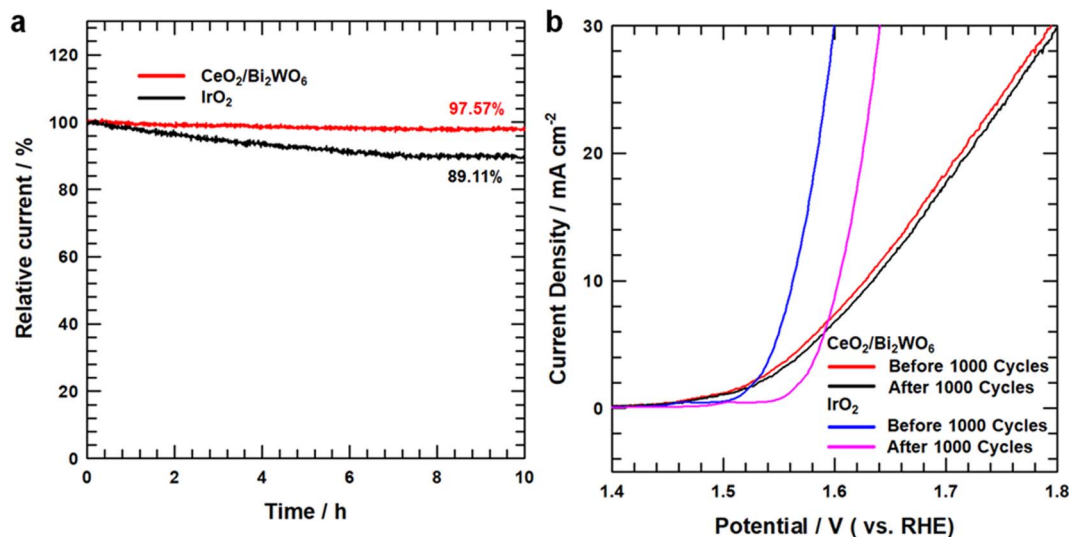


Fig. 7 (a) OER chronoamperometry test of CeO₂/Bi₂WO₆ and IrO₂. (b) OER LSV curves for before and after 1000 cycles CeO₂/Bi₂WO₆ and IrO₂.

As shown in Fig. 5a, the linear sweep voltammetry (LSV) curves showed that CeO₂/Bi₂WO₆ indicated a smaller overpotential of 390 mV, slightly larger than that of CeO₂ (440 mV) and Bi₂WO₆. Besides, to evidence the outstanding OER kinetics of the samples, their Tafel slope were calculated by LSV. As shown in Fig. 5b, CeO₂/Bi₂WO₆ showed a lower Tafel slope (117 mV dec⁻¹) than that of CeO₂ (197.58 mV dec⁻¹) and Bi₂WO₆ (217.33 mV dec⁻¹), and thus CeO₂/Bi₂WO₆ had the fastest kinetic process.^{62,63} Compared with previous studies, the CeO₂/Bi₂WO₆ heterostructure was one of the most efficient Bi₂WO₆-based catalysts (Table S2†). The smallest Tafel slope of CeO₂/Bi₂WO₆ suggested the most favorable OER kinetics, indicating that CeO₂/Bi₂WO₆ possessed an outstanding OER catalytic kinetics. To investigate the OER kinetics of CeO₂/Bi₂WO₆, CeO₂, and Bi₂WO₆, electrochemical impedance spectroscopy (EIS) was conducted, as shown in Fig. 5c. The CeO₂/Bi₂WO₆ nanohybrids had the lowest charge resistance (R_{ct}) than other samples at the interface between the electrolyte and the catalyst. Since R_{ct} represented the rate of charge transfer in OERs,⁶⁴ the smallest R_{ct} value of the CeO₂/Bi₂WO₆ nanohybrid showed the high-speed electron transportation ability of the CeO₂/Bi₂WO₆ nanohybrid during the OER process due to the CeO₂ nanoparticles plentiful in oxygen vacancies evenly grown on Bi₂WO₆ nanosheets.²⁸

To establish why CeO₂/Bi₂WO₆ had better OER activity than that of other samples, we measured double-layer capacitance (C_{dl}) to judge their electrochemically active surface area (ECSA). The ECSA of CeO₂/Bi₂WO₆, CeO₂, and Bi₂WO₆ was revealed by a cyclic voltammetry (CV) method.^{65–67} Fig. 6a–c display the CV curves at different scan rates (10–50 mV s⁻¹) for CeO₂/Bi₂WO₆, CeO₂, and Bi₂WO₆ alkaline solutions, respectively. As the scan speed increased, the current densities of CeO₂/Bi₂WO₆, CeO₂, and Bi₂WO₆ increased accordingly, indicating that the active sites and charge transport capability of CeO₂/Bi₂WO₆, CeO₂, and Bi₂WO₆ increased significantly. In addition, it displayed that CeO₂/Bi₂WO₆ showed the highest capacitive current

compared with CeO₂ and Bi₂WO₆. The C_{dl} and ECSA can be calculated as “ $0.5(I_{anodic} - I_{cathodic})_{1.23 \text{ V vs. RHE}} \text{ (mA cm}^{-2}\text{) / scan rate (mV s}^{-1}\text{)}$ ”, as shown in Fig. 6d, and the C_{dl} of CeO₂/Bi₂WO₆ (1.42 mF cm⁻²) is remarkably higher than that of CeO₂ (0.212 mF cm⁻²) and Bi₂WO₆ (0.159 mF cm⁻²). As a result, the significant activities of C_{dl} and ECSA increased, which might be due to the high oxygen vacancy concentration of the CeO₂/Bi₂WO₆ heterostructure, and CeO₂ nanoparticles equally grown on Bi₂WO₆, which essentially improved the electrocatalytic activity.

The electrocatalytic stability of the CeO₂/Bi₂WO₆ nanohybrids and IrO₂ was tested by chronoamperometry measurements, as shown in Fig. 7a, and the current density of CeO₂/Bi₂WO₆ indicated the unseen modification with respect to the initial value at a retention rate of up to 97.57% after 10 hours of the OER process and showed outstanding stability in an aqueous alkaline medium. In IrO₂, the current retention rate is below 89.11%. Besides, the durability of CeO₂/Bi₂WO₆ was performed by the LSV curves before and after 1000 cycles of the CV curves. As shown in Fig. 7b, the CeO₂/Bi₂WO₆ electrocatalyst showed a negligible decrease in current density, suggesting the good durability of CeO₂/Bi₂WO₆ in alkaline solutions, while IrO₂ shows a significant decrease after 1000 cycles. Because of the synergistic effect of highly stable heterojunctions, the Bi₂WO₆ nanosheets not only guarantee rich active sites, but also ensure a variety of paths for the fast and efficient movement of electrolytes and gases. Meanwhile, the reasonably fixed CeO₂ nanoparticles increase the electrocatalytic activity and enhance the electrical contact with the electrolyte.^{68,69} The above-mentioned electrochemical results confirmed the presence of more active sites, and more efficient and faster electron transport capability in CeO₂/Bi₂WO₆ than those in samples of CeO₂ and Bi₂WO₆, confirming that the CeO₂/Bi₂WO₆ heterostructure catalyst had fine catalytic activity and maintained the excellent stability in an alkaline environment. Therefore, the CeO₂/Bi₂WO₆ heterostructure catalyst is a reasonable strategy to



optimize the OER active sites and durability of Bi₂WO₆-based catalysts.

4. Conclusion

In summary, we have developed a simple strategy to synthesize CeO₂/Bi₂WO₆ nanohybrids with more OER active sites and high durability under alkaline conditions. The characterization and electrochemical measurement results indicated that the CeO₂/Bi₂WO₆ heterostructure electrocatalyst displayed not only more OER catalytic active sites with a smaller overpotential of 390 mV and a lower Tafel slope of 117 mV dec⁻¹ but also durability for 12 h. The distinct heterointerface generates hard bonded electronic effects and the interfacial synergistic effect, making the CeO₂ nanoparticles uniformly anchored onto Bi₂WO₆ for the atoms to expose more active sites, which provided CeO₂/Bi₂WO₆ with electrocatalytic active sites for OERs. Meanwhile, the hard coupled and interfacial synergistic effect really endows the heterojunction structure with good stability for practical application. This CeO₂/Bi₂WO₆ heterostructure catalyst has been developed *via* shape design.

Conflicts of interest

There are no conflicts to declare.

Acknowledgements

This research was supported by the Chung-Ang University Research Scholarship Grants in 2023 and also supported by the National Research Foundation of Korea (NRF) grant funded by the Korea government (MSIT) (2020R1A2C2010445).

References

- 1 J. Chen, X. J. Wu, L. Yin, B. Li, X. Hong, Z. Fan, B. Chen, C. Xue and H. Zhang, One-pot synthesis of CdS nanocrystals hybridized with single-layer transition-metal dichalcogenide nanosheets for efficient photocatalytic hydrogen evolution, *Angew. Chem., Int. Ed. Engl.*, 2015, **54**, 1210–1214.
- 2 P. Chen, K. Xu, S. Tao, T. Zhou, Y. Tong, H. Ding, L. Zhang, W. Chu, C. Wu and Y. Xie, Phase-Transformation Engineering in Cobalt Diselenide Realizing Enhanced Catalytic Activity for Hydrogen Evolution in an Alkaline Medium, *Adv. Mater.*, 2016, **28**, 7527–7532.
- 3 Z. W. Seh, J. Kibsgaard, C. F. Dickens, I. Chorkendorff, J. K. Nørskov and T. F. Jaramillo, Combining theory and experiment in electrocatalysis: Insights into materials design, *Science*, 2017, **355**, 146.
- 4 Q. Song, J. Li, L. Wang, Y. Qin, L. Pang and H. Liu, Stable single-atom cobalt as a strong coupling bridge to promote electron transfer and separation in photoelectrocatalysis, *J. Catal.*, 2019, **370**, 176–185.
- 5 S. Sultan, J. N. Tiwari, A. N. Singh, S. Zhumagali, M. Ha, C. W. Myung, P. Thangavel and K. S. Kim, Single Atoms and Clusters Based Nanomaterials for Hydrogen Evolution, Oxygen Evolution Reactions, and Full Water Splitting, *Adv. Energy Mater.*, 2019, **9**, 1900624.
- 6 X. Zou and Y. Zhang, Noble metal-free hydrogen evolution catalysts for water splitting, *Chem. Soc. Rev.*, 2015, **44**, 5148–5180.
- 7 D. Dong, Z. Wu, J. Wang, G. Fu and Y. Tang, Recent progress in Co9S8-based materials for hydrogen and oxygen electrocatalysis, *J. Mater. Chem. A*, 2019, **7**, 16068–16088.
- 8 G. Fu, X. Jiang, Y. Chen, L. Xu, D. Sun, J.-M. Lee and Y. Tang, Robust bifunctional oxygen electrocatalyst with a “rigid and flexible” structure for air-cathodes, *NPG Asia Mater.*, 2018, **10**, 618–629.
- 9 G. Fu, Y. Tang and J.-M. Lee, Recent Advances in Carbon-Based Bifunctional Oxygen Electrocatalysts for Zn–Air Batteries, *ChemElectroChem*, 2018, **5**, 1424–1434.
- 10 F. Lyu, Q. Wang, S. M. Choi and Y. Yin, Noble-Metal-Free Electrocatalysts for Oxygen Evolution, *Small*, 2019, **15**, 1804201.
- 11 N. T. Suen, S. F. Hung, Q. Quan, N. Zhang, Y. J. Xu and H. M. Chen, Electrocatalysis for the oxygen evolution reaction: recent development and future perspectives, *Chem. Soc. Rev.*, 2017, **46**, 337–365.
- 12 M. Tahir, L. Pan, F. Idrees, X. Zhang, L. Wang, J.-J. Zou and Z. L. Wang, Electrocatalytic oxygen evolution reaction for energy conversion and storage: A comprehensive review, *Nano Energy*, 2017, **37**, 136–157.
- 13 P. Tan, B. Chen, H. Xu, W. Cai, W. He and M. Ni, In-situ growth of Co3O4 nanowire-assembled clusters on nickel foam for aqueous rechargeable Zn-Co3O4 and Zn-air batteries, *Appl. Catal., B*, 2019, **241**, 104–112.
- 14 N. K. Wagh, S. S. Shinde, C. H. Lee, J.-Y. Jung, D.-H. Kim, S.-H. Kim, C. Lin, S. U. Lee and J.-H. Lee, Densely colonized isolated Cu-N single sites for efficient bifunctional electrocatalysts and rechargeable advanced Zn-air batteries, *Appl. Catal., B*, 2020, **268**, 118746.
- 15 Q. Zhao, N. Katyal, I. D. Seymour, G. Henkelman and T. Ma, Vanadium(III) Acetylacetonate as an Efficient Soluble Catalyst for Lithium-Oxygen Batteries, *Angew. Chem., Int. Ed.*, 2019, **58**, 12553–12557.
- 16 X. Zheng, J. Wu, X. Cao, J. Abbott, C. Jin, H. Wang, P. Strasser, R. Yang, X. Chen and G. Wu, N-, P-, and S-doped graphene-like carbon catalysts derived from onium salts with enhanced oxygen chemisorption for Zn-air battery cathodes, *Appl. Catal., B*, 2019, **241**, 442–451.
- 17 J. Sun, H. Xue, Y. Zhang, X. L. Zhang, N. Guo, T. Song, H. Dong, Y. Kong, J. Zhang and Q. Wang, Unraveling the Synergistic Effect of Heteroatomic Substitution and Vacancy Engineering in CoFe2O4 for Superior Electrocatalysis Performance, *Nano Lett.*, 2022, **22**, 3503–3511.
- 18 D. K. Bediako, B. Lassalle-Kaiser, Y. Surendranath, J. Yano, V. K. Yachandra and D. G. Nocera, Structure-activity correlations in a nickel-borate oxygen evolution catalyst, *J. Am. Chem. Soc.*, 2012, **134**, 6801–6809.
- 19 P. Chen, K. Xu, T. Zhou, Y. Tong, J. Wu, H. Cheng, X. Lu, H. Ding, C. Wu and Y. Xie, Strong-Coupled Cobalt Borate Nanosheets/Graphene Hybrid as Electrocatalyst for Water



- Oxidation Under Both Alkaline and Neutral Conditions, *Angew. Chem., Int. Ed.*, 2016, **55**, 2488–2492.
- 20 Q. Shi, C. Zhu, D. Du and Y. Lin, Robust noble metal-based electrocatalysts for oxygen evolution reaction, *Chem. Soc. Rev.*, 2019, **48**, 3181–3192.
 - 21 R. Subbaraman, D. Tripkovic, K. C. Chang, D. Strmcnik, A. P. Paulikas, P. Hirunsit, M. Chan, J. Greeley, V. Stamenkovic and N. M. Markovic, Trends in activity for the water electrolyser reactions on 3d M(Ni,Co,Fe,Mn) hydr(oxy)oxide catalysts, *Nat. Mater.*, 2012, **11**, 550–557.
 - 22 B. Y. Xia, Y. Yan, N. Li, H. B. Wu, X. W. Lou and X. Wang, A metal–organic framework-derived bifunctional oxygen electrocatalyst, *Nat. Energy*, 2016, **1**, 15006.
 - 23 J. Chen, C. Fan, X. Hu, C. Wang, Z. Huang, G. Fu, J. M. Lee and Y. Tang, Hierarchically Porous Co/Cox My (M = P, N) as an Efficient Mott-Schottky Electrocatalyst for Oxygen Evolution in Rechargeable Zn-Air Batteries, *Small*, 2019, **15**, 1901518.
 - 24 K. Zhang, X. Xia, S. Deng, Y. Zhong, D. Xie, G. Pan, J. Wu, Q. Liu, X. Wang and J. Tu, Nitrogen-Doped Sponge Ni Fibers as Highly Efficient Electrocatalysts for Oxygen Evolution Reaction, *Nano-Micro Lett.*, 2019, **11**, 21.
 - 25 R. Zhang, Y.-C. Zhang, L. Pan, G.-Q. Shen, N. Mahmood, Y.-H. Ma, Y. Shi, W. Jia, L. Wang, X. Zhang, W. Xu and J.-J. Zou, Engineering Cobalt Defects in Cobalt Oxide for Highly Efficient Electrocatalytic Oxygen Evolution, *ACS Catal.*, 2018, **8**, 3803–3811.
 - 26 J. Sun, N. Guo, T. Song, Y.-R. Hao, J. Sun, H. Xue and Q. Wang, Revealing the interfacial electron modulation effect of CoFe alloys with CoC encapsulated in N-doped CNTs for superior oxygen reduction, *Adv. Powder Technol.*, 2022, **1**, 100023.
 - 27 J. Sun, H. Xue, N. Guo, T. Song, Y. R. Hao, J. Sun, J. Zhang and Q. Wang, Synergetic Metal Defect and Surface Chemical Reconstruction into NiCo2S4/ZnS Heterojunction to Achieve Outstanding Oxygen Evolution Performance, *Angew. Chem., Int. Ed. Engl.*, 2021, **60**, 19435–19441.
 - 28 J. Li, Z. Liang, Q. Song and X. Xu, Strong-coupled CoOx nanoparticles/Bi2WO6 nanosheets hybrid as electrocatalyst for water oxidation under alkaline conditions, *Mater. Res. Bull.*, 2019, **113**, 152–160.
 - 29 J. Li, Z. Liang, Q. Song and X. Xu, NiFeOx nanosheets tight-coupled with Bi2WO6 nanosheets to improve the electrocatalyst for oxygen evolution reaction, *Appl. Surf. Sci.*, 2019, **478**, 969–980.
 - 30 J. Li, X. Xu, B. Zhang, W. Hou, S. Lv and Y. Shi, Controlled synthesis and fine-tuned interface of NiS nanoparticles/Bi2WO6 nanosheets heterogeneous as electrocatalyst for oxygen evolution reaction, *Appl. Surf. Sci.*, 2020, **526**, 146718.
 - 31 Z.-P. Nie, D.-K. Ma, G.-Y. Fang, W. Chen and S.-M. Huang, Concave Bi2WO6 nanoplates with oxygen vacancies achieving enhanced electrocatalytic oxygen evolution in near-neutral water, *J. Mater. Chem. A*, 2016, **4**, 2438–2444.
 - 32 X. Chia and M. Pumera, Characteristics and performance of two-dimensional materials for electrocatalysis, *Nat. Catal.*, 2018, **1**, 909–921.
 - 33 Y. Zhou, Y. Zhang, M. Lin, J. Long, Z. Zhang, H. Lin, J. C. Wu and X. Wang, Monolayered Bi2WO6 nanosheets mimicking heterojunction interface with open surfaces for photocatalysis, *Nat. Commun.*, 2015, **6**, 8340.
 - 34 D. Yan, Y. Li, J. Huo, R. Chen, L. Dai and S. Wang, Defect Chemistry of Nonprecious-Metal Electrocatalysts for Oxygen Reactions, *Adv. Mater.*, 2017, **29**, 1606459.
 - 35 T. Kwon, M. Jun, J. Joo and K. Lee, Nanoscale hetero-interfaces between metals and metal compounds for electrocatalytic applications, *J. Mater. Chem. A*, 2019, **7**, 5090–5110.
 - 36 M. Li, Y. Wang, Y. Zheng, G. Fu, D. Sun, Y. Li, Y. Tang and T. Ma, Gadolinium-Induced Valence Structure Engineering for Enhanced Oxygen Electrocatalysis, *Adv. Energy Mater.*, 2020, **10**, 1903833.
 - 37 X. Long, W. Qiu, Z. Wang, Y. Wang and S. Yang, Recent advances in transition metal-based catalysts with heterointerfaces for energy conversion and storage, *Mater. Today Chem.*, 2019, **11**, 16–28.
 - 38 J. Mao, P. Liu, C. Du, D. Liang, J. Yan and W. Song, Tailoring 2D MoS2 heterointerfaces for promising oxygen reduction reaction electrocatalysis, *J. Mater. Chem. A*, 2019, **7**, 8785–8789.
 - 39 J. Y. Wang, W. T. Liu, X. P. Li, T. Ouyang and Z. Q. Liu, Strong hydrophilicity NiS2/Fe7S8 heterojunctions encapsulated in N-doped carbon nanotubes for enhanced oxygen evolution reaction, *Chem. Commun.*, 2020, **56**, 1489–1492.
 - 40 Y. Wang, Y. Zou, L. Tao, Y. Wang, G. Huang, S. Du and S. Wang, Rational design of three-phase interfaces for electrocatalysis, *Nano Res.*, 2019, **12**, 2055–2066.
 - 41 Y. Huang, R. Yang, G. Anandhababu, J. Xie, J. Lv, X. Zhao, X. Wang, M. Wu, Q. Li and Y. Wang, Cobalt/Iron(Oxides) Heterostructures for Efficient Oxygen Evolution and Benzyl Alcohol Oxidation Reactions, *ACS Energy Lett.*, 2018, **3**, 1854–1860.
 - 42 J. X. Feng, S. H. Ye, H. Xu, Y. X. Tong and G. R. Li, Design and Synthesis of FeOOH/CeO2 Heterolayered Nanotube Electrocatalysts for the Oxygen Evolution Reaction, *Adv. Mater.*, 2016, **28**, 4698–4703.
 - 43 S. M. Galani, A. Mondal, D. N. Srivastava and A. B. Panda, Development of RuO2/CeO2 heterostructure as an efficient OER electrocatalyst for alkaline water splitting, *Int. J. Hydrog. Energy*, 2020, **45**, 18635–18644.
 - 44 J.-H. Kim, K. Shin, K. Kawashima, D. H. Youn, J. Lin, T. E. Hong, Y. Liu, B. R. Wygant, J. Wang, G. Henkelman and C. B. Mullins, Enhanced Activity Promoted by CeOx on a CoOx Electrocatalyst for the Oxygen Evolution Reaction, *ACS Catal.*, 2018, **8**, 4257–4265.
 - 45 Y. Liu, C. Ma, Q. Zhang, W. Wang, P. Pan, L. Gu, D. Xu, J. Bao and Z. Dai, 2D Electron Gas and Oxygen Vacancy Induced High Oxygen Evolution Performances for Advanced Co3O4/CeO2 Nanohybrids, *Adv. Mater.*, 2019, **31**, 1900062.
 - 46 B. Qiu, C. Wang, N. Zhang, L. Cai, Y. Xiong and Y. Chai, CeO2-Induced Interfacial Co2+ Octahedral Sites and Oxygen Vacancies for Water Oxidation, *ACS Catal.*, 2019, **9**, 6484–6490.



- 47 X. Wang, S. Zhao, Y. Zhang, Z. Wang, J. Feng, S. Song and H. Zhang, CeO₂ nanowires self-inserted into porous Co₃O₄ frameworks as high-performance "noble metal free" hetero-catalysts, *Chem. Sci. J.*, 2016, **7**, 1109–1114.
- 48 Z. Lv, H. Zhou, H. Liu, B. Liu, M. Liang and H. Guo, Controlled assemble of oxygen vacant CeO₂@Bi₂WO₆ hollow magnetic microcapsule heterostructures for visible-light photocatalytic activity, *Chem. Eng. J.*, 2017, **330**, 1297–1305.
- 49 Z. Zou, M. Cai, X. Zhao, J. Huang, J. Du and C. Xu, Defective metal-organic framework derivative by room-temperature exfoliation and reduction for highly efficient oxygen evolution reaction, *J. Mater. Chem. A*, 2019, **7**, 14011–14018.
- 50 Q. Song, J. Li, L. Wang, L. Pang and H. Liu, Controlling the Chemical Bonding of Highly Dispersed Co Atoms Anchored on an Ultrathin g-C₃N₄@Carbon Sphere for Enhanced Electrocatalytic Activity of the Oxygen Evolution Reaction, *Inorg. Chem.*, 2019, **58**, 10802–10811.
- 51 R. Wang, B. Li, Y. Xiao, X. Tao, X. Su and X. Dong, Optimizing Pd and Au-Pd decorated Bi₂WO₆ ultrathin nanosheets for photocatalytic selective oxidation of aromatic alcohols, *J. Catal.*, 2018, **364**, 154–165.
- 52 M. Li, X. Pan, M. Jiang, Y. Zhang, Y. Tang and G. Fu, Interface engineering of oxygen-vacancy-rich CoP/CeO₂ heterostructure boosts oxygen evolution reaction, *Chem. Eng. J.*, 2020, **395**, 125160.
- 53 Y. Zhou, Y. Zhang, M. Lin, J. Long, Z. Zhang, H. Lin, J. C. Wu and X. Wang, Monolayered Bi₂WO₆ nanosheets mimicking heterojunction interface with open surfaces for photocatalysis, *Nat. Commun.*, 2015, **6**, 8340.
- 54 S. Guan, X. Fu, Z. Lao, C. Jin and Z. Peng, NiS–MoS₂ hetero-nanosheet array electrocatalysts for efficient overall water splitting, *Sustain. Energy Fuels*, 2019, **3**, 2056–2066.
- 55 R. Ma, M. Jahurul Islam, D. Amaranatha Reddy and T. K. Kim, Transformation of CeO₂ into a mixed phase CeO₂/Ce₂O₃ nanohybrid by liquid phase pulsed laser ablation for enhanced photocatalytic activity through Z-scheme pattern, *Ceram. Int.*, 2016, **42**, 18495–18502.
- 56 S. Sun, W. Wang and L. Zhang, Facile preparation of three-dimensionally ordered macroporous Bi₂WO₆ with high photocatalytic activity, *J. Mater. Chem.*, 2012, **22**, 19244.
- 57 H. Huang, R. Cao, S. Yu, K. Xu, W. Hao, Y. Wang, F. Dong, T. Zhang and Y. Zhang, Single-unit-cell layer established Bi₂WO₆ 3D hierarchical architectures: Efficient adsorption, photocatalysis and dye-sensitized photoelectrochemical performance, *Appl. Catal., B*, 2017, **219**, 526–537.
- 58 B. Qiu, C. Wang, N. Zhang, L. Cai, Y. Xiong and Y. Chai, CeO₂-Induced Interfacial Co²⁺ Octahedral Sites and Oxygen Vacancies for Water Oxidation, *ACS Catal.*, 2019, **9**, 6484–6490.
- 59 G. Liu, Z. Cui, M. Han, S. Zhang, C. Zhao, C. Chen, G. Wang and H. Zhang, Ambient Electrosynthesis of Ammonia on a Core-Shell-Structured Au@CeO₂ Catalyst: Contribution of Oxygen Vacancies in CeO₂, *Chem*, 2019, **25**, 5904–5911.
- 60 R. Zhang, X. Ren, S. Hao, R. Ge, Z. Liu, A. M. Asiri, L. Chen, Q. Zhang and X. Sun, Selective phosphidation: an effective strategy toward CoP/CeO₂ interface engineering for superior alkaline hydrogen evolution electrocatalysis, *J. Mater. Chem. A*, 2018, **6**, 1985–1990.
- 61 J. Bao, X. Zhang, B. Fan, J. Zhang, M. Zhou, W. Yang, X. Hu, H. Wang, B. Pan and Y. Xie, Ultrathin Spinel-Structured Nanosheets Rich in Oxygen Deficiencies for Enhanced Electrocatalytic Water Oxidation, *Angew. Chem., Int. Ed.*, 2015, **54**, 7399–7404.
- 62 C. Guo, Y. Zheng, J. Ran, F. Xie, M. Jaroniec and S. Z. Qiao, Engineering High-Energy Interfacial Structures for High-Performance Oxygen-Involving Electrocatalysis, *Angew. Chem., Int. Ed.*, 2017, **56**, 8539–8543.
- 63 Y. Jiao, Y. Zheng, M. Jaroniec and S. Z. Qiao, Design of electrocatalysts for oxygen- and hydrogen-involving energy conversion reactions, *Chem. Soc. Rev.*, 2015, **44**, 2060–2086.
- 64 B. Liu, H. Q. Peng, C. N. Ho, H. Xue, S. Wu, T. W. Ng, C. S. Lee and W. Zhang, Mesoporous Nanosheet Networked Hybrids of Cobalt Oxide and Cobalt Phosphate for Efficient Electrochemical and Photoelectrochemical Oxygen Evolution, *Small*, 2017, **13**, 1701875.
- 65 C. C. McCrory, S. Jung, I. M. Ferrer, S. M. Chatman, J. C. Peters and T. F. Jaramillo, Benchmarking hydrogen evolving reaction and oxygen evolving reaction electrocatalysts for solar water splitting devices, *J. Am. Chem. Soc.*, 2015, **137**, 4347–4357.
- 66 F. Lyu, Y. Bai, Z. Li, W. Xu, Q. Wang, J. Mao, L. Wang, X. Zhang and Y. Yin, Self-Templated Fabrication of CoO–MoO₂ Nanocages for Enhanced Oxygen Evolution, *Adv. Funct. Mater.*, 2017, **27**, 1702324.
- 67 X. Shang, K. L. Yan, Y. Rao, B. Dong, J. Q. Chi, Y. R. Liu, X. Li, Y. M. Chai and C. G. Liu, In situ cathodic activation of V-incorporated Ni₃S₂ nanowires for enhanced hydrogen evolution, *Nanoscale*, 2017, **9**, 12353–12363.
- 68 M. Lee, H.-S. Oh, M. K. Cho, J.-P. Ahn, Y. J. Hwang and B. K. Min, Activation of a Ni electrocatalyst through spontaneous transformation of nickel sulfide to nickel hydroxide in an oxygen evolution reaction, *Appl. Catal., B*, 2018, **233**, 130–135.
- 69 L. L. Feng, G. Yu, Y. Wu, G. D. Li, H. Li, Y. Sun, T. Asefa, W. Chen and X. Zou, High-index faceted Ni₃S₂ nanosheet arrays as highly active and ultrastable electrocatalysts for water splitting, *J. Am. Chem. Soc.*, 2015, **137**, 14023–14026.

